Microwave response of fractional quantum Hall droplets with quasiparticle tunneling

Fumihiro Murabayashi,[1,*] Ryotaro Sano,[1] Flavio Ronetti,[2] Jérôme Rech,[2] Thierry Martin,[2] Thibaut Jonckheere,[2] and Takeo Kato[1,†]

[1]*Institute for Solid State Physics, University of Tokyo, Kashiwa 277-8581, Japan*

[2]*Aix Marseille Univ, Université de Toulon, CNRS, CPT, Marseille, France*

(Received 10 March 2026; revised 23 June 2026; accepted 9 July 2026; published 3 August 2026)

We theoretically study microwave absorption spectroscopy of fractional quantum Hall droplets in the presence of quasiparticle tunneling across a quantum point contact. This contact-free probe provides access to collective edge dynamics beyond conventional transport measurements. We develop a nonperturbative path-integral Monte Carlo approach that enables computation of the frequency-dependent response at finite temperature and for arbitrary droplet geometries and benchmark the method against analytical results in the weak-tunneling regime. We find that tunneling produces measurable shifts and broadening of resonance peaks, with systematic dependence on tunneling strength and device geometry. Such shifts and broadenings are not obtained in perturbative treatments acting directly on the response function but emerge when interaction-kernel effects are properly incorporated. Our results indicate experimentally accessible signatures of edge-mode interference and tunneling-induced renormalization of collective excitations and support the use of microwave spectroscopy as a quantitative probe of quasiparticle dynamics in mesoscopic quantum Hall structures.

DOI: 10.1103/rngt-9l21

I. INTRODUCTION

Since its discovery, the fractional quantum Hall effect (FQHE) has had a profound impact on condensed matter physics [1]. Its essence lies in the formation of an incompressible quantum liquid driven by strong electron-electron interactions, and the remarkable agreement between theory and experiment, most notably exemplified by the Laughlin wave function [2], has greatly advanced our understanding of strongly correlated electronic phases. Moreover, the FQHE represents a clear example of topological order that cannot be characterized by any local order parameter, and it has played a decisive role in establishing fundamental concepts in modern topological materials science.

In recent years, renewed attention has been directed toward quasiparticle excitations in fractional quantum Hall (FQH) systems. For the Laughlin state realized at filling $\nu = 1/(2m+1)$ ($m \in \mathbb{Z}$), characterized by a single chiral edge mode encircling the bulk [3], the elementary excitations carry fractional charge. A prominent example is the $\nu = 1/3$ state, in which the quasiparticle contributing to edge transport has been experimentally observed to possess charge $e/3$, as revealed by shot-noise measurements [4,5]. These quasiparticles are known to be Abelian anyons exhibiting exotic fractional statistics, whereby the many-body wave function acquires a phase factor upon exchanging two particles [6–10]. Thanks to significant advances in nanofabrication and measurement technology, this fractional statistic has recently been directly verified through Fabry-Pérot interferometry and nonequilibrium noise measurements [11–13]. Motivated by these achievements, both theoretical and experimental studies on anyonic statistics in FQH systems have intensified rapidly, relying either on interferometry [14–19] or time-domain braiding [20–34].

However, authors of most previous studies have focused on transport properties such as current and nonequilibrium noise in devices where a quantum point contact (QPC) or an interferometer is fabricated in the edge channel [35,36]. Such setups necessarily require attaching source and drain electrodes, making it impossible to avoid the influence of the measurement apparatus itself, including contact resistance and potential fluctuations near the electrodes, on the intrinsic edge structure. Against this background, probing edge excitations via microwave absorption in an isolated quantum Hall droplet [37–39] provides an experimental window fundamentally distinct from conventional transport measurements [40–46]. Related developments in quantum Hall plasmonic and microwave architectures have further highlighted the potential of edge excitations as a resource for spectroscopy and device functionalities [47–49]. Related spectroscopic and contactless approaches have also been discussed for probing quasiparticle dynamics and ac response in quantum Hall systems [50,51]. The setup proposed in Ref. [52] capacitively couples a mesoscopic quantum Hall droplet to a microwave waveguide, allowing direct access to the excitation spectrum of edge modes without any Ohmic contacts. This noninvasive feature effectively eliminates contact-induced disturbances, offering a decisive advantage over transport-based approaches. Furthermore, this method offers several additional benefits that are difficult to realize in transport experiments. First, the resonance frequencies of absorption peaks directly encode the propagation velocity of edge modes, while the number of peaks reflects the number of modes, allowing their physical properties to be determined in a highly

*Contact author: fumihiro@issp.u-tokyo.ac.jp
†Contact author: kato@issp.u-tokyo.ac.jp

 ©2026 American Physical Society

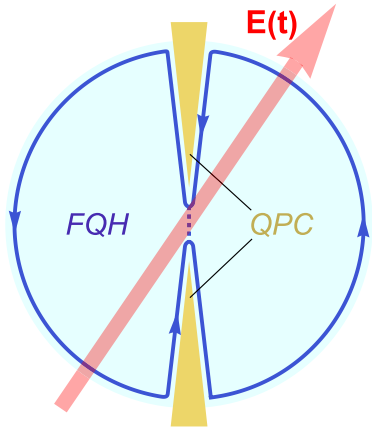


FIG. 1. Schematic view of the setup: a FQH droplet with a chiral edge state (blue line) containing a QPC (yellow), allowing tunneling of fractional quasiparticles. The droplet is driven by a time-varying microwave electric field (large red arrow), assumed spatially uniform over the droplet scale.

direct manner. Second, the set of resonance peaks shows a distinctive dependence on the shape of the droplet, offering a way to explore the geometry of the quantum Hall effect [53]. Finally, when multiple edges are present, by simply varying the droplet size, one can effectively cross the equilibration length of the edge, thereby accessing both the equilibrated regime (single peak) and the nonequilibrated regime (multiple peaks) within the same device [52]. This stands in sharp contrast with transport measurements, where accessing different regimes typically requires altering the positions of electrical contacts [54,55].

In addition, when a QPC is introduced, the absorption peak amplitude exhibits a characteristic interference effect that is linear in the tunneling amplitude, in contrast with the quadratic dependence observed in standard Fabry-Pérot interferometers. This feature greatly enhances sensitivity to quasiparticle charge and statistics. Moreover, contributions from the bulk have frequency and magnetic field dependences distinct from those of the edge [56,57], enabling high-precision extraction of pure edge physics from the absorption spectrum.

In this work, we investigate how quasiparticle tunneling through a QPC modifies the microwave absorption spectrum of a FQH droplet, as shown in Fig. 1. We compute the finite-temperature response nonperturbatively using path-integral Monte Carlo (PIMC), which treats interactions, thermal fluctuations, and tunneling processes on equal footing and allows access to arbitrary droplet geometries. To gain analytical insight, we complement the numerics with perturbative calculations in the tunneling amplitude for an idealized circular geometry and compare the results. Benchmarking against the exact solution for an integer quantum Hall (IQH) droplet at $\nu = 1$ demonstrates the consistency of both the analytical framework and numerical implementation. This combined analysis shows that tunneling strength and temperature induce systematic resonance-peak shifts and linewidth broadening. The peak shifts arise beyond perturbative treatments acting directly on the response function [52], underscoring the importance of considering the interaction kernel in discussing the microwave response. Throughout this paper, we set $\hbar = 1$.

II. MODEL AND FORMULATION

A. Bosonization

We consider a circular FQH state at a finite temperature T (see Fig. 1), hereafter referred to as a FQH droplet. Such a droplet can be realized by applying a negative voltage to appropriately shaped gate electrodes in a two-dimensional electron system. Owing to the bulk energy gap, all low-energy excitations are confined to the boundary and appear as a single unidirectional chiral edge mode, as indicated by the blue line in Fig. 1. Although this edge mode is described by the chiral Luttinger liquid theory [58,59], careful treatment is required for finite-size systems [60,61].

We introduce a coordinate s along the edge of the FQH droplet and define the edge-state region as $0 \leqslant s < L$, where L denotes the circumference. In the bosonization method, the normal-ordered electron density $\rho(s)$ is described with a bosonic field as

$$\rho(s) = \frac{1}{2\pi}\partial_s\varphi(s), \tag{1}$$

where $\varphi(s)$ is a bosonic field obeying the commutation relation

$$[\varphi(s), \varphi(s')] = i\pi\nu\,\mathrm{sgn}(s-s'), \quad (0 < s, s' < L). \tag{2}$$

For a finite system, this bosonic field can be decomposed into two contributions [60,62]

$$\varphi(s) = \varphi_0(s) + \varphi_\mathrm{p}(s), \tag{3}$$

$$\varphi_0(s) = -\nu\vartheta + \frac{2\pi N s}{L}, \tag{4}$$

$$\varphi_\mathrm{p}(s) = \sum_{k>0}\sqrt{\frac{2\pi\nu}{kL}}(b_k e^{iks} + b_k^\dagger e^{-iks})e^{-k\alpha/2}, \tag{5}$$

where $\varphi_0(s)$ and $\varphi_\mathrm{p}(s)$, respectively, denote the zero mode and the periodic part, $N = \int_0^L ds\,\rho(s)$ is the charge operator, ϑ is its conjugate phase operator, and $b_k^\dagger$ (b_k) are bosonic creation (annihilation) operators. The summation runs over discrete wave numbers $k = 2\pi n/L$, with n a positive integer. The canonical commutation relation $[\vartheta, N] = i$ holds by construction.

The quasiparticle annihilation operator is described with the bosonic field as [61]

$$\begin{aligned}\psi_\mathrm{q}(s) &= \frac{1}{\sqrt{2\pi\alpha}}e^{-i\nu\vartheta}e^{2\pi i N s/L}e^{i\varphi_\mathrm{p}(s)} \\ &= \frac{1}{\sqrt{2\pi\alpha}}e^{i\varphi_0(s)+i\pi\nu s/L}e^{i\varphi_\mathrm{p}(s)},\end{aligned} \tag{6}$$

where α is a short-distance cutoff. In the second equality, the operators have been rearranged using the Baker-Campbell-Hausdorff (BCH) formula [63]. The resulting c-number phase factor $e^{i\pi\nu s/L}$ originates from the noncommutativity of ϑ and N.

The Hamiltonian of the chiral edge mode is given by [61]

$$H = \frac{\pi v}{\nu L}[N^2 + (\phi_{\rm AB}/\pi + \nu)N] + \sum_{k>0} vk b_k^\dagger b_k, \tag{7}$$

where v is the velocity of the chiral mode. Here, we have introduced the Aharonov-Bohm (AB) phase $\phi_{\rm AB} = 2\pi\Phi/\Phi_0$, where Φ is the magnetic flux through the droplet, and $\Phi_0 = h/e^*$ is the flux quantum corresponding to the quasiparticle charge $e^* = \nu e$. In the presence of the AB phase, the quasiparticle operator is replaced as

$$\psi_{\rm q}(s) = \frac{1}{\sqrt{2\pi\alpha}} e^{i\varphi_0(s) + i\phi_{\rm AB} s/L + i\pi\nu s/L} e^{i\varphi_{\rm p}(s)}. \tag{8}$$

In this work, we only consider the $N = 0$ sector. This is justified when the effect of thermal fluctuations on the charge number N can be neglected. To this end, we consider the low-temperature regime ($k_{\rm B}T \ll 2\pi v/L$) and choose a phase $\phi_{\rm AB}$ close to $-\pi\nu$ where the thermal fluctuations of N are minimized. Furthermore, the phase operator ϑ can be dropped as we consider quasiparticle tunneling within a single edge mode, which does not modify the total number of quasiparticles on the edge. Therefore, the quasiparticle annihilation operator is simplified as

$$\psi_{\rm q}(s) = \frac{1}{\sqrt{2\pi\alpha}} e^{i\varphi_{\rm p}(s)}. \tag{9}$$

In what follows, we denote $\varphi_{\rm p}(s)$ as $\varphi(s)$ to keep the notation as simple as possible.

B. Effective action

In the following, we derive the effective action by applying the path-integral formalism to the nonzero mode. The imaginary-time action of the edge modes is given as follows [64]:

$$S_{\rm edge}[\varphi] = \frac{1}{4\pi\nu}\int_0^L ds \int_0^\beta d\tau\, \partial_s\varphi(i\partial_\tau\varphi + v\partial_s\varphi), \tag{10}$$

where L is the circumference of the circular FQH droplet, and $\beta = 1/k_{\rm B}T$ is the inverse temperature.

Next, we consider the effect of quasiparticle tunneling at a QPC. In this study, we focus on quasiparticle tunneling between positions s_1 and s_2 along the edge of the droplet. For a tunneling amplitude λ_r, the action describing the quasiparticle tunneling is given by

$$\begin{aligned} S_{\rm tun}[\varphi] &= -\lambda_r \int_0^\beta d\tau\, [\psi_{\rm q}^\dagger(s_2,\tau)\psi_{\rm q}(s_1,\tau) + {\rm H.c.}] \\ &= -V\int_0^\beta d\tau\, \cos[\varphi(s_1,\tau) - \varphi(s_2,\tau)], \end{aligned} \tag{11}$$

where in the last step, we set $V = \lambda_r/\pi\alpha$. From this, the action of the system is $S_{\rm edge}[\varphi] + S_{\rm tun}[\varphi]$, and the partition function is expressed using path integrals as

$$Z \propto \int \mathcal{D}\varphi\, e^{-S_{\rm edge}[\varphi] - S_{\rm tun}[\varphi]}. \tag{12}$$

For the calculation of the response function, we employ the generating functional with an auxiliary real field $\lambda(\tau)$, which allows us to carry out the Gaussian integration everywhere except at the positions s_1 and s_2

$$Z \propto \int \mathcal{D}\varphi\, \mathcal{D}\lambda\, \mathcal{D}\phi\, e^{-S_{\rm edge}[\varphi] - S_{\rm tun}[\varphi] - S_\lambda[\varphi,\lambda,\phi]}, \tag{13}$$

where we introduced the action involving the newly defined fields

$$S_\lambda[\varphi,\lambda,\phi] = i\int_0^\beta d\tau\, \lambda(\tau)[\varphi(s_1,\tau) - \varphi(s_2,\tau) - \phi(\tau)]. \tag{14}$$

Here, $S_\lambda[\varphi,\lambda,\phi]$ enforces the constraint between the fields at s_1 and s_2.

After performing a Fourier transform, completing the square, and carrying out Gaussian integrations over the fields λ and φ, the generating functional reduces to an action depending only on the local field $\phi(\tau)$, which corresponds to the effective action $S_{\rm eff}[\phi]$ of the system

$$Z \propto \int \mathcal{D}\phi\, e^{-S_{\rm eff}[\phi]}, \tag{15}$$

$$S_{\rm eff}[\phi] = S_0[\phi] + S_{\rm tun}[\phi]. \tag{16}$$

Here, $S_0[\phi]$ and $S_{\rm tun}[\phi]$ represent the contributions from the edge states and quasiparticle tunneling, respectively, and are given by

$$S_0[\phi] = \sum_{\omega_n} \frac{|\phi_n|^2}{4\beta\Lambda_n}, \tag{17}$$

$$S_{\rm tun}[\phi] = -V\int_0^\beta d\tau\, \cos[\phi(\tau)]. \tag{18}$$

Here, ϕ_n is a Fourier transformation of $\phi(\tau)$

$$\phi(\tau) = \frac{1}{\beta}\sum_{\omega_n} \phi_n e^{-i\omega_n\tau}, \tag{19}$$

and $\omega_n \equiv 2\pi n/\beta$ denotes the bosonic Matsubara frequencies. Also, Λ_n is a function dependent on s_1 and s_2, which is given by

$$\Lambda_n = \frac{2\pi\nu}{\omega_n} \frac{\sinh\left(\frac{\omega_n|s_1-s_2|}{2v}\right)\sinh\left(\frac{\omega_n(L-|s_1-s_2|)}{2v}\right)}{\sinh\left(\frac{\omega_n L}{2v}\right)}. \tag{20}$$

For a detailed derivation, see Appendix A. One readily sees from Eq. (17) that Λ_n is directly related to the propagator of the effective bosonic field ϕ.

C. Response function

To formulate the microwave response function of the droplet, we first define the polarization of the edge states as follows:

$$\hat{P} = \int_0^L ds\, y(s)\rho(s), \tag{21}$$

where $y(s)$ denotes the y coordinate of the edge of the droplet, along which the direction of the oscillating electric field is aligned. We assume that the microwave has a sufficiently long wavelength so that the electric field remains constant over the scale of the droplet.

In this work, we focus on an idealized setup in which the droplet remains circular, and particle (or quasiparticle)

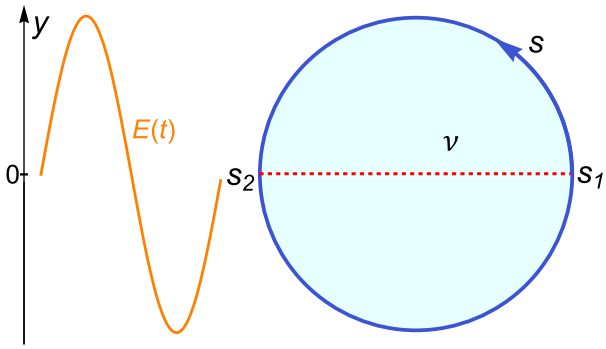


FIG. 2. Schematic of a quantum Hall droplet with circular geometry at filling ν. The coordinate y is defined parallel to the oscillating microwave electric field, while the coordinate s parametrizes the circumference of the droplet. The points s_1 and s_2 denote the positions of the QPCs. Although a realistic droplet would exhibit constrictions at these locations, we consider an idealized setup in which the droplet remains circular and particle (or quasiparticle) tunneling occurs at s_1 and s_2.

tunneling occurs at s_1 and s_2, as shown in Fig. 2, serving as a representative example. For a circular droplet with circumference L, $y(s)$ is given by

$$y(s) = \frac{L}{2\pi}\sin\left(\frac{2\pi s}{L}\right). \tag{22}$$

In the rest of this section, we formulate the microwave response for this setup, whereas the extension to different geometries can be carried out analogously and will be discussed in Sec. V.

The Hamiltonian describing the interaction between the microwave electric field and the edge states is then given by

$$\hat{H}^{(\mathrm{ex})}(t) = -E(t)\hat{P} = -E(t)\int_0^L ds\, y(s)\rho(s). \tag{23}$$

We define the expectation value of the polarization change due to the external field $E(t)$ as $\delta\langle\hat{P}(t)\rangle \equiv \langle\hat{P}(t)\rangle - \langle\hat{P}\rangle$. The Fourier transforms of the electric field and the polarization change are then given by

$$E(t) = \int_{-\infty}^{\infty}\frac{d\omega}{2\pi}E(\omega)e^{-i\omega t}, \tag{24}$$

$$\delta\langle\hat{P}(t)\rangle = \int_{-\infty}^{\infty}\frac{d\omega}{2\pi}\delta P(\omega)e^{-i\omega t}. \tag{25}$$

The linear response of the polarization to the electric field is summarized in the form $\delta P(\omega) = \epsilon^R(\omega)E(\omega)$ by linear response theory, where the susceptibility $\epsilon^R(\omega)$ is given by the Fourier transform of the retarded polarization correlation function $\epsilon^R(t) = i\Theta(t)\langle[\hat{P}(t), \hat{P}(0)]\rangle$. Here, $\hat{P}(t)$ denotes the time evolution of the polarization in the absence of the external field (in the Heisenberg picture). The susceptibility $\epsilon^R(\omega)$ can be calculated from the imaginary-time evolution of the polarization as follows:

$$\epsilon^R(\omega) = \epsilon(i\omega_n \to \omega + i\delta), \tag{26}$$

$$\epsilon(i\omega_n) = \int_0^\beta d\tau\,\epsilon(\tau)e^{i\omega_n\tau}, \tag{27}$$

$$\epsilon(\tau) = \langle T_\tau\hat{P}(\tau)\hat{P}(0)\rangle. \tag{28}$$

Here, $\hat{P}(\tau)$ represents the imaginary-time evolution of the polarization in the absence of the external field, which can be expressed by replacing the charge density $\rho(s)$ in Eq. (21) with its imaginary-time evolution $\rho(s,\tau)$. Because the microwave absorption intensity is directly related to $\mathrm{Im}\,\epsilon^R(\omega)$ through the fluctuation-dissipation theorem, we restrict our attention to this quantity in what follows.

From Eqs. (27) and (28), the response function in the Matsubara representation is calculated as

$$\epsilon(i\omega_n) = \int_0^L dsds'\, y(s)y(s')S_{\rho\rho}(s,s',i\omega_n). \tag{29}$$

Here, $S_{\rho\rho}(s,s',i\omega_n)$ is given as the Fourier transform of the imaginary-time density-density correlation function of the edge state $S_{\rho\rho}(s,s',\tau) \equiv \langle T_\tau\rho(s,\tau)\rho(s',0)\rangle$. The charge density $\rho(s,\tau)$ is rewritten with the bosonic field as $\rho(s,\tau) = (2\pi)^{-1}\partial_s\varphi(s,\tau)$. To evaluate $S_{\rho\rho}(s,s',\tau)$, we introduce a source term coupled to an external field $\eta(s,\tau)$ into the generating functional defined in Sec. II A, as follows:

$$Z[\eta] \propto \int \mathcal{D}\varphi\,\mathcal{D}\lambda\,\mathcal{D}\phi\, e^{-S_{\mathrm{edge}}[\varphi]-S_{\mathrm{tun}}[\varphi]-S_\lambda[\varphi,\lambda,\phi]-S_\eta[\varphi]}, \tag{30}$$

$$S_\eta[\varphi] = \frac{1}{2\pi}\int_0^\beta d\tau\int_0^L ds\,\eta(s,\tau)\,\partial_s\varphi(s,\tau). \tag{31}$$

The correlation function can be calculated directly from the generating functional $Z[\eta]$, introduced in Eq. (30), as

$$\begin{aligned} S_{\rho\rho}(s,s',\tau,\tau') &\equiv \frac{1}{4\pi^2}\langle T_\tau\partial_s\varphi(s,\tau)\partial_{s'}\varphi(s',\tau')\rangle \\ &= \frac{1}{Z[\eta]}\frac{\delta^2 Z[\eta]}{\delta\eta(s,\tau)\delta\eta(s',\tau')}\bigg|_{\eta=0}. \end{aligned} \tag{32}$$

D. Response function in a circular droplet

By functional differentiation of the resulting generating functional, we can obtain the explicit expression for the density correlation function

$$S_{\rho\rho}(s,s',i\omega_n) = S^{(0)}_{\rho\rho}(s,s',i\omega_n) + \beta\Phi(i\omega_n)A(s,s',i\omega_n), \tag{33}$$

where one has

$$S^{(0)}_{\rho\rho}(s,s',i\omega_n) = \frac{\nu}{2\pi L}\sum_{k\neq 0}\frac{k}{\nu k - i\omega_n}e^{ik(s-s')}, \tag{34}$$

$$\Phi(i\omega_n) = \frac{2}{\beta\Lambda_n}\left(-1 + \frac{\langle\phi_n\phi_{-n}\rangle}{2\beta\Lambda_n}\right), \tag{35}$$

$$A(s,s',i\omega_n) = \frac{\nu^2}{4L^2}\sum_{i,j=1}^{2}(-1)^{i+j}\sum_{k,k'\neq 0}\frac{e^{ik(s-s_i)}}{\nu k - i\omega_n}\frac{e^{-ik'(s'-s_j)}}{\nu k' - i\omega_n}. \tag{36}$$

In Eq. (35), we introduced the correlator for the local fields

$$\langle\phi_n\phi_{-n}\rangle = \frac{1}{Z[0]}\int\mathcal{D}\phi\;\phi_n\phi_{-n}e^{-S_0[\phi]-S_{\mathrm{tun}}[\phi]}. \tag{37}$$

For details of the calculation, see Appendix B. Using the results of Eqs. (33)–(36), the integration in Eq. (29) yields the following response function in the Matsubara formalism:

$$\epsilon(i\omega_n) = \epsilon_0(i\omega_n) + \delta\epsilon(i\omega_n), \tag{38a}$$

$$\epsilon_0(i\omega_n) = \frac{vL^2}{16\pi^2}\left[\frac{1}{\omega_T + i\omega_n} + \frac{1}{\omega_T - i\omega_n}\right], \tag{38b}$$

$$\delta\epsilon(i\omega_n) = \frac{\beta v^2 L^2}{16\pi^2}\Phi(i\omega_n)\left[\frac{1}{(\omega_T - i\omega_n)^2} + \frac{1}{(\omega_T + i\omega_n)^2} - \frac{\cos\frac{2\pi(s_1+s_2)}{L}}{\omega_T}\left(\frac{1}{\omega_T + i\omega_n} + \frac{1}{\omega_T - i\omega_n}\right)\right]. \tag{38c}$$

Here, $\epsilon_0(i\omega_n)$ corresponds to the response function of the free droplet without a QPC, while $\delta\epsilon(i\omega_n)$ characterizes the modification of the response function due to the quasiparticle tunneling at a QPC. In the absence of a QPC, $\delta\epsilon(i\omega_n)$ vanishes, and we see from the expression in Eq. (38b) that the resonance corresponds to a peak at frequency $\omega = \omega_T \equiv 2\pi v/L$, which is the characteristic frequency of the droplet. We notice that, to obtain Eq. (38c), we made the assumption $|s_1 - s_2| = L/2$.

To obtain the response function in the presence of tunneling at the QPC, one needs to evaluate the bosonic correlator $\Phi(i\omega_n)$ [Eq. (35)]. This cannot be done exactly in the general case. In this work, we use two different methods to obtain $\Phi(i\omega_n)$ [and thus $\epsilon(i\omega_n)$]: On the one hand, we analytically calculate second-order perturbation in the tunneling strength V; on the other hand, we use the numerical method of PIMC for arbitrary tunneling amplitudes. The PIMC method allows us not only to obtain results beyond the perturbative limit but also to confirm the perturbative results in their regime of validity.

From this point onward and unless mentioned otherwise, we focus on a symmetric circular droplet, with a QPC connecting the positions $s_1 = 0$ and $s_2 = L/2$ (see Fig. 2).

E. Perturbation theory

When the tunneling strength V is small enough, it is possible to perform a perturbative expansion of the bosonic correlator $\Phi(i\omega_n)$ of Eq. (35). This leads to

$$\epsilon(i\omega_n) = \epsilon_0(i\omega_n) + V\epsilon^{(1)}(i\omega_n) + V^2\epsilon^{(2)}(i\omega_n) + O(V^3). \tag{39}$$

Since the zeroth-order response function ϵ_0 exhibits narrow resonance peaks at $\pm\omega_T$, quasiparticle tunneling at the QPC is expected to change both the resonance frequencies and the peak widths. However, a bare perturbative expansion of the form in Eq. (39) does not allow one to directly extract these quantities since the peak positions and linewidths are determined by the zeros of the inverse response function rather than by additive corrections to $\epsilon(i\omega_n)$ itself. To properly characterize these effects, we therefore introduce the interaction kernel $\Gamma(i\omega_n)$ as follows:

$$\Gamma(i\omega_n) \equiv \epsilon_0^{-1}(i\omega_n) - \epsilon^{-1}(i\omega_n). \tag{40}$$

Within this formulation, the real and imaginary parts of $\Gamma(\omega)$ directly encode the tunneling-induced peak shifts and the corresponding changes in the linewidth. This represents a significant methodological distinction from the earlier analysis of Ref. [52], in which microwave absorption spectroscopy was proposed as a probe of quasiparticle tunneling and the tunneling effect was treated through a direct first-order perturbative expansion of the response function. Within that treatment, the resonance-peak shifts were not discussed explicitly. By contrast, our perturbative treatment of the interaction kernel $\Gamma(\omega)$ makes it possible to capture the peak shift due to quasiparticle tunneling. Another important difference is that, in the present work, we include contributions up to second order in perturbation theory. While the peak shift already appears at first order within our interaction-kernel formulation, changes in the linewidth emerge only at second order. Considering these second-order contributions allows us to describe features intrinsic to fractional quantum Hall edge dynamics, such as the renormalization of the linewidth.

Using Eqs. (35), (38c), and (39), we obtain for $\Gamma(i\omega_n)$ up to second order in V

$$\Gamma^{(2)}(i\omega_n) = -V\frac{64\pi^2}{L^2}e^{-\bar{\Lambda}} - V^2\frac{32\pi^2 e^{-2\bar{\Lambda}}}{L^2} \times\left[8\nu\left(\frac{1}{\omega_T - i\omega_n} + \frac{1}{\omega_T + i\omega_n}\right) + \mathcal{P}_+(0) + \mathcal{P}_-(0) - \mathcal{P}_+(i\omega_n) + \mathcal{P}_-(i\omega_n) - 2\beta\right]. \tag{41}$$

Here, $\mathcal{P}_\pm(i\omega_n)$ and $\bar{\Lambda}$ are defined as

$$\mathcal{P}_\pm(i\omega_n) \equiv \int_0^\beta d\tau\, e^{i\omega_n\tau} e^{\pm\frac{2}{\beta}\sum_p \Lambda_p \cos\omega_p\tau}, \tag{42}$$

$$\bar{\Lambda} \equiv \frac{1}{\beta}\sum_{\omega_m}\Lambda_m, \tag{43}$$

and one can show that $e^{-\bar{\Lambda}} \simeq (\pi\alpha/L)^\nu$. Once $\Gamma^{(2)}$ is computed, the response function $\epsilon_p(i\omega_n)$ in the perturbative regime is then obtained as

$$\epsilon_{\rm p}(i\omega_n) = \frac{1}{\epsilon_0^{-1}(i\omega_n) - \Gamma^{(2)}(i\omega_n)}. \tag{44}$$

After performing the analytic continuation to the real frequency, the real part of $\Gamma^{(2)}(\omega + i\delta)$ corresponds to the shift in the position of the resonance peaks, while the imaginary part yields the broadening and deformation of the peaks. From Eq. (41), one readily sees that the first-order term in $\Gamma^{(2)}(\omega + i\delta)$ is purely real, thus leading to a simple shift of the resonance peaks, while the second-order term yields both a shift and a widening. Note that the order n term contains a factor $e^{-n\bar{\Lambda}} = (\pi\alpha/L)^{\nu n}$. As $(\pi\alpha/L) \ll 1$, this is a small factor that guarantees the validity of the perturbation expansion. As this factor increases when ν decreases, one can expect that higher-order terms in the perturbative expansion will be more important for a given V as ν decreases (see Sec. IV).

F. PIMC method

In this study, we also evaluate $\Phi(i\omega_n)$ using the PIMC method and thereby obtain a numerically exact response

function. In this approach, the partition function is represented as an imaginary-time path integral over $\phi(\tau)$, and representative paths are sampled with the weight determined by the Euclidean action. From the $\Phi(i\omega_n)$ obtained via PIMC, we compute $\Gamma(i\omega_n)$ and perform numerical analytic continuation to finite real frequencies using the Padé approximation, thereby obtaining the response function on the real-frequency axis from Eq. (40). Since the PIMC results include higher-order effects in the coupling strength, this method enables us to access the response not only in the region dominated by second-order perturbations but also in regimes where higher-order effects become significant.

The PIMC procedure is summarized as follows. In the numerical implementation, the imaginary-time interval $[0, \beta)$ is discretized as $\tau_l = l\Delta\tau$ $(l = 0, 1, 2, \ldots, N-1)$, with $\Delta\tau = \beta/N$, and the path is represented by $\phi(\tau_l)$. With this discretization, the effective action is approximated as

$$S_{\rm eff}[\phi] = S_0[\phi] + S_{\rm tun}[\phi], \tag{45}$$

$$S_0[\phi] = \sum_{n=-N/2+1}^{N/2} \frac{|\phi_n|^2}{4\beta\Lambda_n}, \tag{46}$$

$$S_{\rm tun}[\phi] = -V\Delta\tau \sum_{l=0}^{N-1} \cos\left[\phi(\tau_l)\right]. \tag{47}$$

The Fourier transform defined in Eq. (19) is accordingly modified to

$$\phi(\tau_l) = \frac{1}{\beta} \sum_{n=-N/2+1}^{N/2} \phi_n e^{-i\omega_n\tau_l}. \tag{48}$$

Here, the Fourier components satisfy the relation $\phi_{-n} = \phi_n^*$. The Monte Carlo update is carried out in the frequency domain. Starting from a configuration $\{\phi_n\}$, we successively choose a frequency index k in the range $[0, N/2]$ and propose a new value of ϕ_k drawn from the Gaussian distribution associated with the quadratic action $e^{-S_0[\phi]}$. The original and proposed configurations are then transformed to the imaginary-time domain, and the change in the tunneling action is evaluated as

$$\Delta S = S_{\rm tun}[\{\phi(\tau_l)\}^{(\rm new)}] - S_{\rm tun}[\{\phi(\tau_l)\}]. \tag{49}$$

The proposed update is accepted according to the Metropolis criterion with probability $\min(1, e^{-\Delta S})$. A complete sweep over all frequency components constitutes one Monte Carlo step. Repeating this procedure generates imaginary-time paths distributed according to the Boltzmann weight $e^{-S_{\rm eff}[\phi]}$, from which the correlation functions are evaluated by importance sampling.

III. RESULTS FOR THE IQH DROPLET CASE

In this section, we present the analytical calculation for the IQH droplet with a filling factor $\nu = 1$, where the edge state is described by a noninteracting chiral electron system. We benchmark the consistency of the perturbative and PIMC results against the analytic solution.

We consider a finite edge state in an IQH droplet, as illustrated in Fig. 3. At the QPC, which connects the points $s = 0$ and $s = L/2$, electrons can either be transmitted or reflected to the opposite point. We define the S matrix at the QPC as

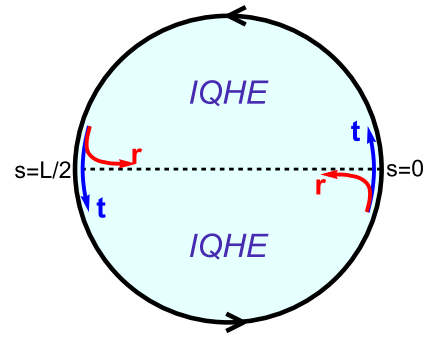


FIG. 3. Schematic and notation used in the exact IQH effect calculation. The droplet is circular, with perimeter L. The QPC connects the points at $s = 0$ and $s = L/2$ and is characterized by reflection and transmission amplitudes r and t.

$$\hat{S} = \begin{pmatrix} t & -ir \\ -ir & t \end{pmatrix}, \tag{50}$$

where r and $t = \sqrt{1-r^2}$ are the reflection and transmission amplitudes, respectively (see Fig. 3), which are determined from the quasiparticle tunneling λ_r (see Appendix C). We note that $t = 1$ corresponds to the absence of a QPC ($\lambda_r = 0$). As mentioned in Sec. II A, a uniform magnetic field is applied to the droplet, and as electrons move along the edge, they acquire a phase factor $e^{i\phi_{\rm AB}s/L}$ due to the AB effect. The AB phase is given by $\phi_{\rm AB} = 2\pi\Phi/\Phi_0$, as stated previously, where the flux quantum is $\Phi_0 = h/e$.

By imposing the twisted boundary conditions that account for the AB effect, the wave number is discretized as

$$k_{n,j} = \frac{4\pi}{L}(n + \delta_j), \quad (n \in \mathbb{Z},\ j = 1, 2), \tag{51a}$$

$$\delta_1 = \frac{\chi}{2\pi} - \frac{\phi_{\rm AB}}{4\pi}, \tag{51b}$$

$$\delta_2 = \frac{1}{2} - \frac{\chi}{2\pi} - \frac{\phi_{\rm AB}}{4\pi}, \tag{51c}$$

where $\chi = \arctan(r/t) \in [0, \pi/2]$ denotes the coupling strength at the QPC (for a detailed derivation, see Appendix C). In the absence of the QPC ($r = 0$), the energy-level spacing is simply given by an integer multiple of $2\pi/L$, reflecting the edge-state length L. When the QPC is introduced, the energy levels are divided into two groups $k_{n,1}$ and $k_{n,2}$, having their wave numbers shifted in opposite directions by a factor $\chi/2\pi$. The AB phase $\phi_{\rm AB}$ induces uniform shifts of both wave numbers $k_{n,1}$ and $k_{n,2}$, which have the same effect as changing the chemical potential.

The electrons that pass through the QPC at $s = L/2$ acquire $\Theta_j = (-1)^j\chi$ for the wave number $k_{n,j}$ (see Appendix C). Accordingly, the imaginary-time evolution of the electron field operator $\psi(s, \tau)$ is expressed as

$$\psi(s, \tau) = \frac{1}{\sqrt{L}} \sum_n \sum_{j=1,2} e^{ik_{n,j}s - vk_{n,j}\tau} g_j(s) c_{n,j}, \tag{52}$$

$$g_j(s) = \begin{cases} 1, & (s < L/2), \\ e^{i\Theta_j}, & (s > L/2). \end{cases} \tag{53}$$

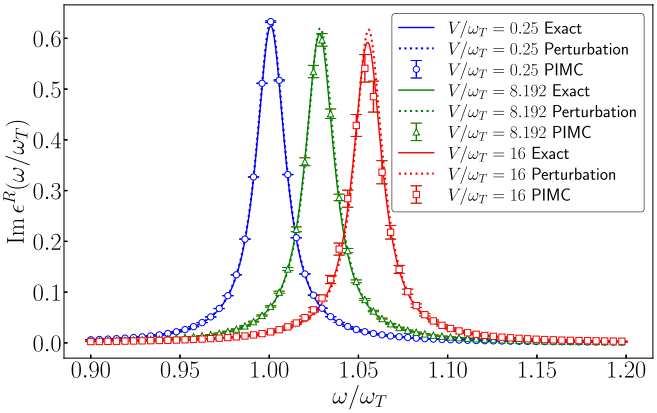


FIG. 4. Imaginary part of the susceptibility $\mathrm{Im}\,\epsilon^R(\omega)$ for the $\nu = 1$ IQH droplet, shown in units of L^2/ω_T. The temperature is set to $T/\omega_T = 0.1$. Solid and dashed lines show the results of scattering theory [Eq. (55)] and second-order perturbation theory [Eqs. (41)–(44)], respectively, while symbols with error bars represent numerical data obtained using the PIMC method. Dimensionless coupling strengths are $V/\omega_T = 0.25$, 8.192, and 16. For visual clarity, delta functions are broadened into Lorentzians with linewidth $\delta = \omega_T/100$.

The imaginary-time response function is given by

$$S_{\rho\rho}(s, s', \tau) = \langle \psi^\dagger(s, \tau)\psi(s', 0)\rangle\langle \psi(s, \tau)\psi^\dagger(s', 0)\rangle. \quad (54)$$

for $0 < \tau < \beta$. By substituting Eqs. (52)–(54) into Eq. (29) and performing the integration over s and s', the imaginary part of the susceptibility is calculated as

$$\mathrm{Im}\,\epsilon^R(\omega) = \frac{L^2 \sin^2\chi}{16\pi^3} \sum_{m,n} \frac{f(vk_{n,1}) - f(vk_{m,2})}{(n - m + \chi/\pi)^2(n - m + \chi/\pi - 1)^2} \times \{\delta[\omega + v(k_{n,1} - k_{m,2})] - \delta[\omega - v(k_{n,1} - k_{m,2})]\}. \quad (55)$$

The response function is determined by transitions between the different eigenstates with eigenenergies $vk_{n,1}$ and $vk_{m,2}$, as indicated by the delta function $\delta[\omega \pm v(k_{n,1} - k_{m,2})]$ (see also Appendix C). Due to the factor $f(vk_{n,1}) - f(vk_{m,2})$, only transition from occupied states to unoccupied states possible at zero temperature.

This exact expression allows us to check the correctness of our two calculation methods: the second-order perturbation and the PIMC simulation. To make comparison easier, the delta function in Eq. (55) is replaced with a Lorentzian function with a small width δ. This corresponds to the analytic continuation $i\omega_n \to \omega + i\delta$ with a finite value of δ. Figure 4 shows the response function $\mathrm{Im}\,\epsilon^R(\omega)$ for the case of a circular droplet at $\nu = 1$. It compares the results of all three methods: the exact theoretical treatment of Eq. (55), the results obtained from second-order perturbation theory [Eqs. (41)–(44)], and the numerical results computed using the PIMC method. In this comparison, a clear shift of the peak at $\omega = \omega_T = 2\pi v/L$ toward higher frequencies is observed as the coupling strength increases, and all three results show good overall agreement within the range of coupling strengths considered. For larger coupling strengths, particularly at $V/\omega_T = 16$, the Monte Carlo and exact theoretical results remain in good agreement, whereas the second-order perturbation begins to show a slight deviation in intensity. We found that second-order perturbation agrees well with the exact theoretical treatment for moderate coupling strengths, while the PIMC simulations accurately reproduce the exact theoretical results over the entire range considered.

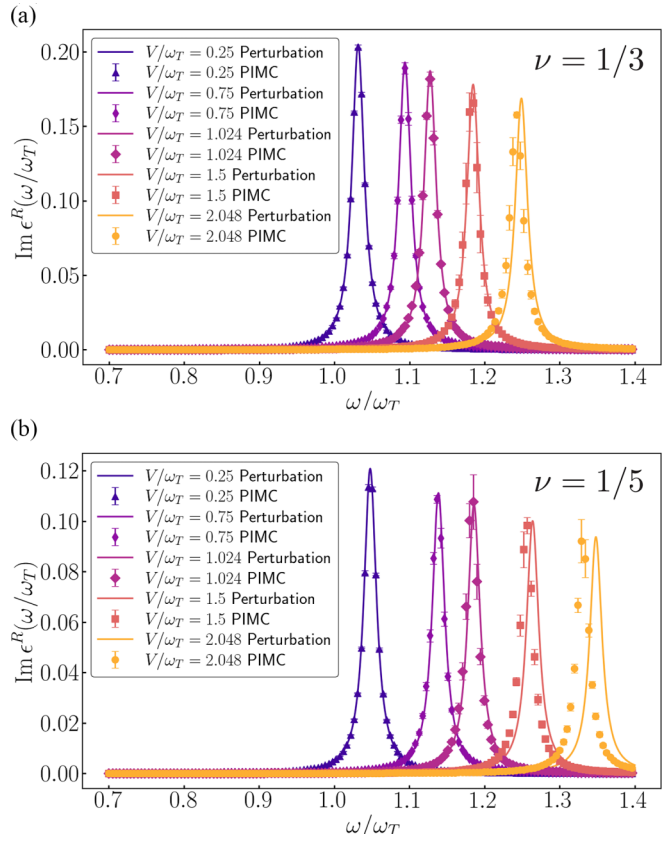


FIG. 5. Imaginary part of the susceptibility $\mathrm{Im}\,\epsilon^R(\omega)$ for FQH droplets with (a) $\nu = 1/3$ and (b) $\nu = 1/5$ at temperature $T/\omega_T = 0.1$. Solid lines show results from second-order perturbation theory, whereas symbols with error bars represent data obtained using PIMC. Coupling strengths are $V/\omega_T = 0.25, 0.75, 1.024, 1.5,$ and 2.048. A finite broadening $\delta = \omega_T/100$ is used.

IV. RESULTS FOR THE FQH DROPLET CASE

Next, we discuss the behavior of $\mathrm{Im}\,\epsilon^R(\omega)$ for a FQH droplet, based on perturbation theory and numerical calculations using the PIMC method, as an exact analytical calculation is not available in this case. Through this comparison, we further examine how the deviation between the perturbative and PIMC results depends on the filling factor.

Figures 5(a) and 5(b) show the behavior of $\mathrm{Im}\,\epsilon^R(\omega)$ for $\nu = 1/3$ and $1/5$, respectively, with varying dimensionless coupling strength $V/\omega_T = 0.25$, 0.75, 1.024, 1.5, and 2.048 at a fixed temperature of $T/\omega_T = 0.1$. To make the peak shift clearer, we have used a finite broadening factor $\delta = \omega_T/100$ in the analytic continuation. The solid lines represent the perturbative results, while the plotted points denote the PIMC results. As in the case of the IQH droplet, the resonance

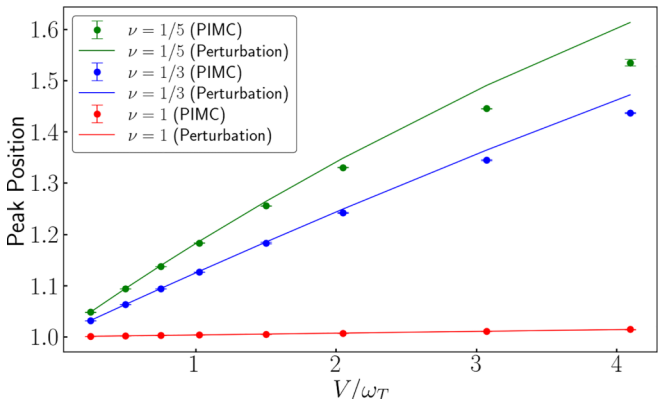


FIG. 6. Dependence of resonance-peak positions on tunneling strength for filling fractions $\nu = 1/5$, $1/3$, and 1. Solid curves denote results from second-order perturbation theory, while symbols represent PIMC results.

peak shifts toward higher frequencies as the coupling strength increases. In both figures, this peak shift is more pronounced than in the IQH droplet. Moreover, for a given value of the coupling strength V, the shift is found to be larger for $\nu = 1/5$ than for $\nu = 1/3$. As seen from Eq. (41), the first- and second-order terms are accompanied by factors of $e^{-\tilde{\Lambda}}$ and $e^{-2\tilde{\Lambda}}$, respectively. These factors get larger as ν decreases since $e^{-\tilde{\Lambda}} \simeq (\pi\alpha/L)^{\nu}$. Therefore, it can be concluded that the effect of the coupling strength becomes more significant for smaller ν.

In Fig. 5, as the coupling strength increases, a noticeable deviation between the PIMC and second-order perturbative results begins to appear. This deviation emerges at smaller coupling strengths for $\nu = 1/5$ than for $\nu = 1/3$, indicating that the $\nu = 1/5$ state is more sensitive to the coupling strength and exhibits higher-order effects more prominently. Figure 6 shows the dependence of the peak position on the coupling strength for $\nu = 1$, $1/3$, and $1/5$. The solid lines represent the peak shifts obtained from the second-order perturbation results, while the plotted points correspond to those obtained from the PIMC calculations. Within the range of coupling strengths shown, the peak for $\nu = 1$ exhibits only a small shift, and the perturbative and PIMC results agree well. As discussed above, the peak shift becomes larger as ν decreases from $1/3$ to $1/5$. As the coupling strength increases, a noticeable deviation appears between the perturbative and PIMC results, with the deviation being more significant for $\nu = 1/5$ than for $\nu = 1/3$. This observation suggests that higher-order effects become increasingly important for smaller filling factors and that such effects are successfully captured by the PIMC calculations.

Next, Figs. 7(a) and 7(b) show the temperature dependence of $\mathrm{Im}\,\epsilon^R(\omega)$ for $\nu = 1/3$ and $1/5$. The coupling strength is fixed at $V/\omega_T = 1.5$. As in Fig. 5, the solid lines represent the perturbative results, while the plotted points denote the PIMC results. For both $\nu = 1/3$ and $1/5$, the increase in linewidth with rising temperature is commonly observed in both the perturbative and PIMC results. In the present formulation, phonon effects are not considered, indicating that the linewidth broadening is caused by thermal fluctuations. In the PIMC results, a low-energy shift with increasing temperature

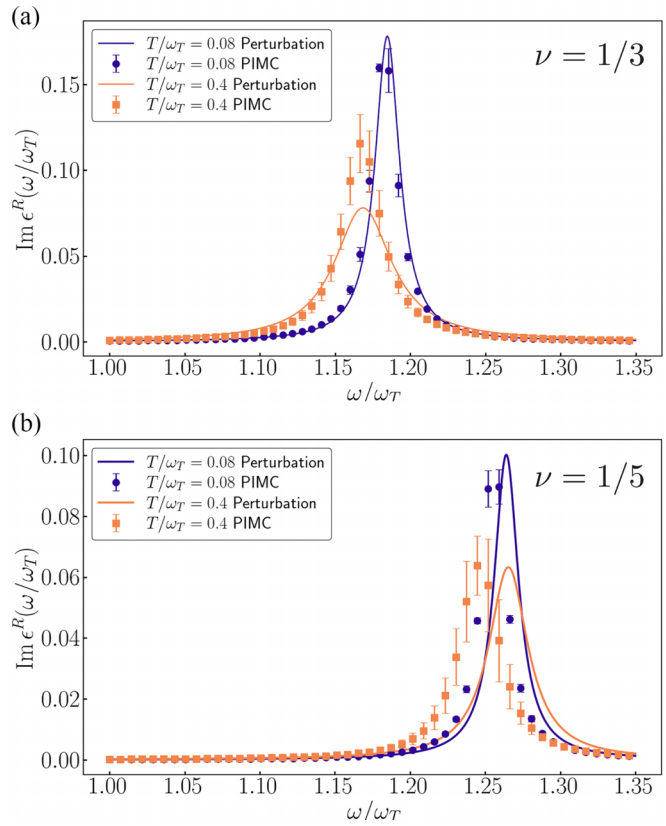


FIG. 7. Imaginary part of the susceptibility $\mathrm{Im}\,\epsilon(\omega)$ at $T/\omega_T = 0.08$ (blue) and 0.4 (orange) for FQH droplets with (a) $\nu = 1/3$ and (b) $\nu = 1/5$ at coupling strength $V/\omega_T = 1.5$. A broadening factor $\delta = \omega_T/100$ is used.

is observed for both $\nu = 1/3$ and $1/5$. While the perturbative result for $\nu = 1/3$ exhibits a similar behavior, the one for $\nu = 1/5$ shows no noticeable peak shift as the temperature increases. From this result, the low-energy peak shift observed for $\nu = 1/5$ is considered to be caused by higher-order effects.

V. RESULTS FOR THE REALISTIC GEOMETRY CASE

We now present the dielectric response in a more realistic geometry. So far, for simplicity, we have focused on a circular droplet geometry. In the following, we consider a geometry constructed from two overlapping circles of equal radius R, whose centers are laterally offset by $2a$, as illustrated in Fig. 8. Equation (29) provides the general expression for the response function, and by using the edge profile $y(s)$ corresponding to this droplet shape, the calculation can be carried out in the same manner as in the circular case. Importantly, the geometry dependence enters only through the edge profile $y(s)$, while the bosonic correlation function is geometry independent. Therefore, responses for different geometries can be obtained using a single set of Monte Carlo data for the bosonic correlator, without repeating the numerically expensive simulations.

In Fig. 8, the radius of each circle R is given by $R = L/[4(\pi - \gamma)]$, as obtained from the geometry shown in the figure. Furthermore, from the relation $R\cos\gamma = a$, it follows that the angle γ is determined once the distance between the centers of the two circles is specified. At this point, $y(s)$ can

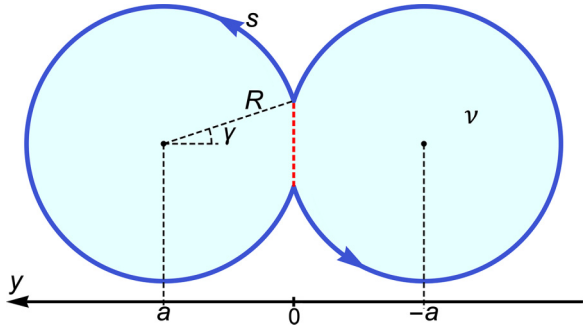


FIG. 8. Schematic of a realistic droplet geometry composed of two circular arcs joined at a junction. The QPC is formed by a constriction at this junction, whose opening angle is denoted by γ.

be expressed as follows:

$$y(s) = \begin{cases} R[\cos\gamma - \cos(R^{-1}s + \gamma)], & (s < L/2), \\ -R[\cos\gamma - \cos(R^{-1}s + 3\gamma)], & (s > L/2). \end{cases} \tag{56}$$

By performing the integration in Eq. (29), the response function in Matsubara space is obtained as follows:

$$\epsilon^{\text{real}}(i\omega_n) = \epsilon_0^{\text{real}}(i\omega_n) + \delta\epsilon^{\text{real}}(i\omega_n), \tag{57a}$$

$$\epsilon_0^{\text{real}}(i\omega_n) = \frac{8\nu R^{-2}\cos^2\gamma}{\pi L} \times \sum_{l\in\mathbb{Z}} \frac{1}{\Delta_l\left(R^{-2} - \Delta_l^2\right)^2(v\Delta_l - i\omega_n)}, \tag{57b}$$

$$\delta\epsilon^{\text{real}}(i\omega_n) = \frac{16\beta\nu^2 R^{-2}\cos^2\gamma}{L^2}\Phi(i\omega_n) \times \left[\sum_{l\in\mathbb{Z}} \frac{1}{\Delta_l\left(R^{-2} - \Delta_l^2\right)(v\Delta_l - i\omega_n)}\right]^2, \tag{57c}$$

where $\Delta_l \equiv 2(2l-1)\pi/L$. The resulting susceptibility displays a set of peaks at energies set by $v\Delta_l$, with $l \in \mathbb{Z}$. Therefore, since $v\Delta_l = (2l-1)\omega_T$, it follows that, in the geometry shown in Fig. 8, multiple peaks appear at odd multiples of ω_T. This geometry reduces to that of the circular droplet with QPCs located at $s = 0$ and $s = L/2$ when $\gamma = \pi/2$. Indeed, Eqs. (57b) and (57c) coincide with Eqs. (38b) and (38c) in the limit $\gamma \to \pi/2$ for $s_1 + s_2 = L/2$.

Figure 9 shows the calculated $\text{Im}\,\epsilon^{\text{R}}(\omega)$ for the $\nu = 1/3$ FQH droplet with the geometry illustrated in Fig. 8. It is confirmed that the secondary peak appears at three times the frequency of ω_T. As indicated from Eqs. (57b) and (57c), the amplitude decays rapidly when increasing the mode index l. In addition, as the coupling strength increases, a peak shift occurs, similar to the case of the circular droplet. The direction of the shift depends on the peak position. The peak located at $\omega/\omega_T = 1$ shifts toward higher frequencies, while the one at $\omega/\omega_T = 3$ shifts toward lower frequencies.

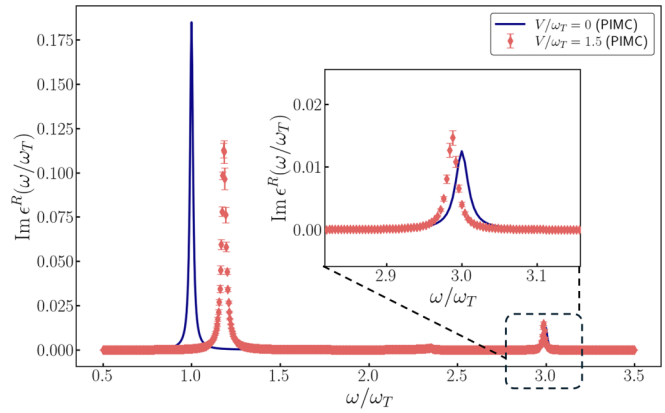


FIG. 9. Imaginary part of the susceptibility $\text{Im}\,\epsilon^R(\omega)$ at $T/\omega_T = 0.1$ for a $\nu = 1/3$ FQH droplet with the geometry shown in Fig. 8. The solid curve shows the analytical result at zero tunneling strength $V/\omega_T = 0$, while symbols represent PIMC data at $V/\omega_T = 1.5$. The constriction of the droplet is controlled by the geometric angle γ, which is set to $\gamma = \pi/15$. A broadening $\delta = \omega_T/100$ is used. The inset shows a magnified view of the secondary peak.

VI. SUMMARY

In this work, we investigated the microwave response of FQH droplets containing a QPC using a combination of PIMC simulations and perturbation theory up to second order in the tunneling strength. For IQH droplets, we benchmarked the approach against results obtained from quantum scattering theory, confirming the consistency of the response functions in regimes where analytical solutions are available.

We demonstrated that quasiparticle tunneling induces resonance peak shifts as well as thermal linewidth broadening, which were not addressed in the original proposal of Ref. [52]. We further showed that these peak shifts can be discussed reasonably only when the interaction kernel of the response function is considered, highlighting the limitations of bare perturbative expansions. The resulting behavior exhibits a clear dependence on the filling factor, reflecting the evolution of correlation strength in FQH states and explaining the increasing deviation between PIMC and finite-order perturbative results at smaller filling factors.

Because the PIMC framework naturally incorporates higher-order contributions beyond perturbation theory while retaining geometric and thermal flexibility, it provides a robust tool for evaluating microwave response in regimes where perturbative approaches become inaccurate. These results establish microwave spectroscopy as a quantitative probe of quasiparticle dynamics and collective edge excitations in mesoscopic quantum Hall droplets and offer a practical pathway for connecting theoretical modeling with experimental measurements across a wide range of filling factors and device geometries. The proposed spectroscopy protocol is compatible with current quantum Hall experimental platforms, particularly in view of recent developments in gate-tunable edge-magnetoplasmon resonators and the high degree of control achieved over QPCs [49]. Within the model considered here, quasiparticle (anyon) braiding effects are not the dominant mechanism influencing the microwave response. Extending the PIMC framework to regimes where braiding plays a central role in microwave resonances represents a promising direction for future investigation. Another natural extension of the present work is the investigation of FQH states with multiple edge channels, such as those of the Jain sequence,

where interchannel interactions and charge fractionalization may lead to a richer microwave absorption spectrum.

ACKNOWLEDGMENTS

We thank G. Fève, G. Ménard, and F. Parmentier for useful discussions on experimental aspects. F.M. is supported by the International Graduate Program of Innovation for Intelligent World of the University of Tokyo. This research is supported by Japan Science and Technology Agency (JST) SPRING, Grant No. JPMJSP2108. R.S. is supported by the Hirose Foundation and the Murata Science and Education Foundation. T.K. acknowledges the support of the Japan Society for the Promotion of Science (JSPS KAKENHI Grant No. JP24K06951). F.M. and T.K. acknowledge the support of the JST ASPIRE Program No. JPMJAP2410. This work was carried out in the framework of the project "ANY-HALL" (Grant No. ANR-21-CE30-0064-03). We acknowledge funding from the Agence Nationale de la Recherche under the France 2030 programme, Reference No. ANR-22-PETQ-0012, and from the ERC Advanced Grant "ASTEC" (Grant No. 101096610). This French-Japanese collaboration is supported by the CNRS International Research Project "Excitations in Correlated Electron Systems driven in the GigaHertz range".

DATA AVAILABILITY

The data and code that support the findings of this article are openly available in Ref. [65].

APPENDIX A: DERIVATION OF THE EFFECTIVE ACTION

In this appendix, we present the procedure for deriving the effective action. We first introduce the Fourier transforms of the bosonic field $\varphi(s,\tau)$ and the auxiliary field $\lambda(\tau)$ as

$$\varphi(s,\tau)=\frac{1}{L\beta}\sum_{k\neq 0}\sum_{\omega_n}\varphi_{k,n}e^{iks-i\omega_n\tau}, \tag{A1}$$

$$\lambda(\tau)=\frac{1}{\beta}\sum_{\omega_n}\lambda_n e^{-i\omega_n\tau}. \tag{A2}$$

Using these definitions, the imaginary-time actions $S_{\rm edge}[\varphi]$ and $S_\lambda[\varphi,\lambda,\phi]$, originally defined in Eqs. (10) and (14), respectively, can be rewritten as

$$S_{\rm edge}[\varphi]=\frac{1}{L\beta}\sum_{k\neq 0}\sum_{\omega_n}\frac{k(vk-i\omega_n)}{4\pi v}|\varphi_{k,n}|^2, \tag{A3}$$

$$S_\lambda[\varphi,\lambda,\phi]=\frac{i}{L\beta}\sum_{k\neq 0}\sum_{\omega_n}\lambda_{-n}[(e^{iks_1}-e^{iks_2})\varphi_{k,n}-L\phi_n]. \tag{A4}$$

Since the total action $S_{\rm edge}[\varphi]+S_\lambda[\varphi,\lambda,\phi]+S_{\rm tun}[\phi]$ is quadratic in $\varphi_{k,n}$, the bosonic field can be integrated out in the partition function defined in Eq. (13), yielding

$$Z\propto\int\mathcal{D}\lambda\,\mathcal{D}\phi\,e^{-S_0'[\phi,\lambda]-S_{\rm tun}[\phi]}, \tag{A5}$$

$$S_0'[\phi,\lambda]=\frac{\pi v}{L\beta}\sum_{k\neq 0}\sum_{\omega_n}\frac{|e^{iks_1}-e^{iks_2}|^2}{k(vk-i\omega_n)}|\lambda_n|^2-\frac{i}{2\beta}\sum_{\omega_n}(\lambda_{-n}\phi_n+\lambda_n\phi_{-n}). \tag{A6}$$

Because the effective action $S_0'[\phi,\lambda]$ is quadratic in λ_n, the auxiliary field λ_n can be further integrated out, leading to

$$Z\propto\int\mathcal{D}\phi\,e^{-S_0[\phi]-S_{\rm tun}[\phi]}, \tag{A7}$$

$$S_0[\phi]=\sum_{\omega_n}\frac{|\phi_n|^2}{4\beta\Lambda_n}. \tag{A8}$$

Here, the coefficient Λ_n is given by

$$\Lambda_n=\frac{\pi v}{L}\sum_{k\neq 0}\frac{|e^{iks_1}-e^{iks_2}|^2}{k(vk-i\omega_n)}. \tag{A9}$$

Noting that the summation over the wave number is taken for $k=2\pi m/L$ with m being a nonzero integer, Λ_n can be evaluated as

$$\Lambda_n=\frac{vL}{\pi v}\sum_{m=1}^{\infty}\frac{1-\cos 2\pi m(s_1-s_2)/L}{m^2+(\omega_nL/2\pi v)^2}. \tag{A10}$$

Finally, by using the identity

$$\sum_{m=1}^{\infty}\frac{\cos nx}{n^2+a^2}=\frac{\pi}{2a}\frac{\cosh a(\pi-x)}{\sinh a\pi}-\frac{1}{2a^2}, \tag{A11}$$

valid for $0\leqslant x\leqslant 2\pi$, we arrive at the expression given in Eq. (20).

APPENDIX B: DERIVATION OF THE DENSITY CORRELATION FUNCTION

In this appendix, we present the derivation of the density-density correlation function. As discussed in Sec. II C, the charge density $\rho(s,\tau)$ can be expressed in terms of the bosonic field $\varphi(s,\tau)$ as

$$\rho(s,\tau)=\frac{1}{2\pi}\partial_s\varphi(s,\tau)=\frac{1}{L\beta}\sum_{\omega_n}\sum_{k\neq 0}\frac{ik}{2\pi}\varphi_{k,n}e^{iks-i\omega_n\tau}. \tag{B1}$$

Accordingly, the density-density correlation function is written as

$$S_{\rho\rho}(s,s',\tau)=\left(\frac{i}{2\pi L\beta}\right)^2\sum_{\omega_n}\sum_{k,k'\neq 0}kk'\langle\varphi_{k,n}\varphi_{k',-n}\rangle\times e^{iks+ik's'-i\omega_n\tau}. \tag{B2}$$

The source term associated with the external field $\eta(s,\tau)$ in the action in Eq. (31) can be rewritten, after Fourier transformation, as

$$S_\eta[\varphi]=\frac{1}{L\beta}\sum_{\omega_n}\sum_{k\neq 0}\frac{ik}{2\pi}\eta_{-k,-n}\varphi_{k,n}, \tag{B3}$$

where $\eta_{-k,-n}=\eta_{k,n}^*$. From Eqs. (30) and (B3), we therefore obtain

$$\frac{1}{Z[0]}\frac{\delta^2Z[\eta]}{\delta\eta_{-k,-n}\delta\eta_{-k',n}}\bigg|_{\eta=0}=\left(\frac{i}{2\pi L\beta}\right)^2kk'\langle\varphi_{k,n}\varphi_{k',-n}\rangle. \tag{B4}$$

In complete analogy with the derivation of the effective action in Eq. (13), the fields $\varphi(s,\tau)$ and $\lambda(\tau)$ in the generating

functional in Eq. (30) can be integrated out by Gaussian integration, leaving only the local field degree of freedom $\phi(\tau)$. At this stage, the generating functional takes the form

$$Z[\eta] \propto \int \mathcal{D}\phi\, e^{-S_{\rm eff}[\phi]-S_{\eta,1}[\phi,\eta]-S_{\eta,2}[\eta]}, \tag{B5}$$

where

$$S_{\eta,1}[\phi,\eta] = -\sum_{\omega_n}\sum_{k\neq 0}\frac{\nu(e^{-iks_2}-e^{-iks_1})}{2i\beta L\Lambda_n(\nu k-i\omega_n)}\eta_{-k,-n}\phi_n, \tag{B6}$$

$$S_{\eta,2}[\eta] = -\frac{\nu}{4\pi\beta L}\sum_{\omega_n}\left(\sum_{k\neq 0}\frac{k}{\nu k-i\omega_n}|\eta_{k,n}|^2 - \sum_{k,k'\neq 0}\frac{\nu(e^{-iks_1}-e^{-iks_2})(e^{ik's_1}-e^{ik's_2})}{\Lambda_n(\nu k-i\omega_n)(\nu k'-i\omega_n)}\eta^*_{k,n}\eta_{k',n}\right). \tag{B7}$$

Using Eqs. (B5)–(B7), we obtain

$$\frac{1}{Z[0]}\frac{\delta^2 Z[\eta]}{\delta\eta_{-k,-n}\delta\eta_{-k',n}}\bigg|_{\eta=0} = \left\langle\frac{\delta^2 e^{-S_{\eta,1}[\phi,\eta]}}{\delta\eta_{-k,-n}\delta\eta_{-k',n}}\right\rangle_{\eta=0} + \left\langle\frac{\delta^2 e^{-S_{\eta,2}[\eta]}}{\delta\eta_{-k,-n}\delta\eta_{-k',n}}\right\rangle_{\eta=0}, \tag{B8}$$

where $\langle\cdots\rangle = Z[0]^{-1}\int\mathcal{D}\phi\,(\cdots)e^{-S_{\rm eff}[\phi]}$. Evaluating each term on the right-hand side of Eq. (B8), we find

$$\left\langle\frac{\delta^2 e^{-S_{\eta,1}[\phi,\eta]}}{\delta\eta_{-k,-n}\delta\eta_{-k',n}}\right\rangle_{\eta=0} = \frac{\langle\phi_n\phi_{-n}\rangle}{\beta^2\Lambda_n^2}\tilde{A}(i\omega_n), \tag{B9}$$

$$\left\langle\frac{\delta^2 e^{-S_{\eta,2}[\eta]}}{\delta\eta_{-k,-n}\delta\eta_{-k',n}}\right\rangle_{\eta=0} = -\frac{2\tilde{A}(i\omega_n)}{\beta\Lambda_n} + \frac{\nu k}{2\pi L\beta(\nu k-i\omega_n)}\delta_{k,-k'}. \tag{B10}$$

Here, we have introduced

$$\tilde{A}(i\omega_n) \equiv \sum_{i,j=1}^{2}\frac{\nu^2(-1)^{i+j+1}e^{-iks_i-ik's_j}}{4\beta^2L^2\Lambda_n^2(\nu k-i\omega_n)(\nu k'+i\omega_n)}. \tag{B11}$$

Combining these results with Eqs. (B2) and (B4), the density-density correlation function is obtained as

$$S_{\rho\rho}(s,s',\tau) = \sum_{\omega_n}\frac{2e^{-i\omega_n\tau}}{\beta\Lambda_n}\left[-1+\frac{\langle\phi_n\phi_{-n}\rangle}{2\beta\Lambda_n}\right]A(s,s',i\omega_n) + \frac{\nu}{2\pi\beta L}\sum_{\omega_n}\sum_{k\neq 0}\frac{k}{\nu k-i\omega_n}e^{ik(s-s')-i\omega_n\tau}. \tag{B12}$$

The function $A(s,s',i\omega_n)$ is identical to that defined in Eq. (36). Finally, by performing a Fourier transform with respect to imaginary time, we recover the expressions given in Eqs. (33)–(35).

APPENDIX C: DETAILED CALCULATIONS FOR IQH DROPLETS

In this appendix, we present the derivation of the results for IQH droplets given in Sec. III. Throughout this appendix, we work in first quantization. In the absence of the QPC, the edge state of the IQH droplet is described by a noninteracting chiral electron channel, which satisfies the Schrödinger equation

$$-iv\partial_s\psi(s) = E\psi(s), \quad (0\leqslant s<L). \tag{C1}$$

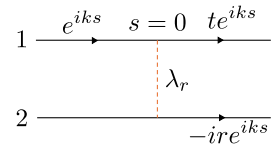


FIG. 10. Schematic for a wave function on two transmission channels for an electron incident from channel 1 toward the QPC.

To relate the strength of quasiparticle tunneling λ_r to the transmission and reflection amplitudes t and r, we introduce $\psi_1(s)=\psi(s)$ and $\psi_2(s)=\psi(s+L/2)$, both of which are discontinuous at $s=0$ (see Fig. 10). In the limit $L\to\infty$, the Schrödinger equation in the presence of the QPC reads

$$(-iv\partial_s\hat{I}+\lambda_r\delta(s)\hat{\sigma}_x)\begin{pmatrix}\psi_1(s)\\ \psi_2(s)\end{pmatrix} = E\begin{pmatrix}\psi_1(s)\\ \psi_2(s)\end{pmatrix}. \tag{C2}$$

Here, $\hat{I}$ is the identity matrix, and $\hat{\sigma}_x$ is the x-component Pauli matrix. Consider the scattering ansatz

$$\psi_1(s) = \begin{cases}e^{iks}, & (s<0),\\ te^{iks}, & (s>0),\end{cases} \tag{C3}$$

$$\psi_2(s) = \begin{cases}0, & (s<0),\\ -ire^{iks}, & (s>0).\end{cases} \tag{C4}$$

Substituting Eqs. (C3) and (C4) into Eq. (C2) and integrating across $x=0$ yields

$$t = \frac{1-\lambda_r^2/4v^2}{1+\lambda_r^2/4v^2}, \tag{C5}$$

$$r = \frac{\lambda_r/v}{1+\lambda_r^2/4v^2}. \tag{C6}$$

Thus, $r>0$ for $\lambda_r>0$ ($\tilde{V}>0$). In comparison with the PIMC simulation, the short-distance cutoff is identified as $\alpha=v\Delta\tau$ (see also Sec. II F).

For a finite system, the eigenwave numbers and eigenenergies are denoted by $k_{n,j}$ and $E_{n,j}=vk_{n,j}$, respectively. The wave function of the chiral edge mode takes the form

$$\psi(s) = \begin{cases}e^{iks+i\phi_{\rm AB}s/L}, & (0<s<L/2),\\ e^{iks+i\phi_{\rm AB}s/L+i\Theta}, & (L/2<s<L),\end{cases} \tag{C7}$$

where Θ is a phase shift at the QPC, and $\phi_{\rm AB}$ is an AB phase induced by the external magnetic field. The normalization is set to unity since the energy eigenvalues do not depend on it. The incident and outgoing wave functions at the QPCs are given by

$$\psi_{\rm in}(0) = \psi(L-0) = e^{ikL+i\phi_{\rm AB}+i\Theta}, \tag{C8}$$

$$\psi_{\rm out}(0) = \psi(0+0) = 1, \tag{C9}$$

$$\psi_{\rm in}(L/2) = \psi(L/2-0) = e^{ikL/2+i\phi_{\rm AB}/2}, \tag{C10}$$

$$\psi_{\rm out}(L/2) = \psi(L/2+0) = e^{ikL/2+i\phi_{\rm AB}/2+i\Theta}. \tag{C11}$$

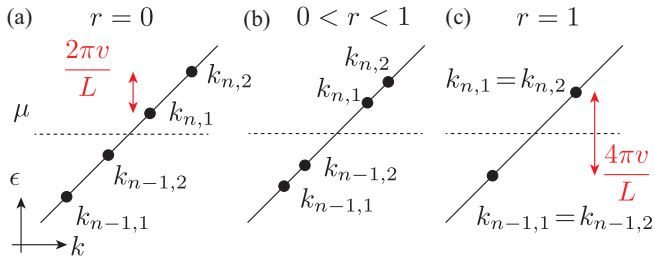


FIG. 11. Schematic of energy levels for (a) $r = 0$ ($\chi = 0$), (b) $0 < r < 1$ ($0 < \chi < \pi/2$), and (c) $r = 1$ ($\chi = \pi/2$). The horizontal axis represents the electron wave number, and the vertical axis the energy. The dashed line denotes the chemical potential.

Applying the S matrix in Eq. (50), we obtain

$$\begin{pmatrix} \psi_{\rm out}(0) \\ \psi_{\rm out}(L/2) \end{pmatrix} = \begin{pmatrix} t & -ir \\ -ir & t \end{pmatrix} \begin{pmatrix} \psi_{\rm in}(0) \\ \psi_{\rm in}(L/2) \end{pmatrix}. \tag{C12}$$

Substituting Eqs. (C8)–(C11) and eliminating $e^{i\Theta}$, one obtains

$$x^2 - 2irx - 1 = 0, \tag{C13}$$

where $x = e^{ikL/2 + i\phi_{\rm AB}/2}$. The solutions are $x = ir \pm t = e^{i\chi}, e^{i(\pi-\chi)}$, where $\tan\chi = r/t$ $(0 \leqslant \chi \leqslant \pi/2)$. The wave numbers are thus discretized as $k_{n,j} = 4\pi(n + \delta_j)/L$, where $\delta_1 = (2\chi - \phi_{\rm AB})/4\pi$ and $\delta_2 = 1/2 - (2\chi + \phi_{\rm AB})/4\pi$ denote the QPC-induced shifts. Figure 11 shows a schematic energy diagram for $\phi_{\rm AB} = -\pi$. In the absence of the QPC ($r = 0$), the wave number reduces to $k = 2\pi(m + 1/2)/L$, as expected. On the other hand, for the decoupled droplets ($r = 1$), the wave number becomes doubly degenerate, as $k = 4\pi(n + 1/2)/L$. The phase shifts follow from Eqs. (C8)–(C11) and are given by

$$\Theta_j = \begin{cases} -\chi, & (j = 1), \\ \chi, & (j = 2). \end{cases} \tag{C14}$$

Using these eigenfunctions, the electron field operators are written as

$$\psi(x,\tau) = \frac{1}{\sqrt{L}} \sum_n \sum_{j=1,2} e^{ik_{n,j}x - vk_{n,j}\tau} g_j(x) c_{n,j}, \tag{C15}$$

$$\psi^\dagger(x,\tau) = \frac{1}{\sqrt{L}} \sum_n \sum_{j=1,2} e^{-ik_{n,j}x + vk_{n,j}\tau} g_j^*(x) c_{n,j}^\dagger, \tag{C16}$$

where $c_{n,j}$ ($c_{n,j}^\dagger$) denotes the annihilation (creation) operator and $g_j(x)$ is defined by

$$g_j(x) = \begin{cases} 1, & (x < L/2), \\ e^{i\Theta_j}, & (x > L/2). \end{cases} \tag{C17}$$

Using the identity

$$y(x) = \frac{L}{2\pi} \sin\frac{2\pi x}{L} = \sum_{\eta=\pm1} \frac{\eta L}{4\pi i} \exp\left(\frac{2\pi i \eta x}{L}\right), \tag{C18}$$

the imaginary-time susceptibility reads

$$\epsilon(\tau) = \frac{1}{L^2} \sum_{m,n} \sum_{j,j'=1}^{2} e^{v(k_{n,j} - k_{m,j'})\tau} \times f(vk_{n,j})(1 - f(vk_{m,j'}))I_{n,j,m,j'} I^*_{n,j,m,j'}, \tag{C19}$$

where $f(\epsilon) = (e^{\beta\epsilon} + 1)^{-1}$ is the Fermi-Dirac distribution function, and $I_{n,j,m,j'}$ is defined as

$$I_{n,j,m,j'} = \frac{L}{4\pi i} \sum_{\eta=\pm1} \int_0^L dx\, g_j^*(x) g_{j'}(x) e^{2\pi i \eta x/L - i(k_{n,j} - k_{m,j'})x}. \tag{C20}$$

Carrying out the integration yields

$$I_{n,1,m,1} = I_{n,2,m,2} = 0, \tag{C21}$$

$$I_{n,2,m,1} = \frac{iL^2 e^{i\chi} \sin\chi/4\pi^2}{(m - n + \chi/\pi)(m - n - 1 + \chi/\pi)}, \tag{C22}$$

$$I_{n,1,m,2} = -\frac{iL^2 e^{-i\chi} \sin\chi/4\pi^2}{(n - m + \chi/\pi)(n - m - 1 + \chi/\pi)}. \tag{C23}$$

After Fourier transformation and analytic continuation ($i\omega_n \to \omega + i\delta$), we obtain Eq. (55).

APPENDIX D: DETAILED CALCULATIONS OF PERTURBATION

Our starting point is the effective action derived in Appendix A. An auxiliary field $\xi(\tau) = \beta^{-1} \sum_n \xi_n e^{-i\omega_n \tau}$ is introduced. The generating functional then reads

$$Z[\xi] = \int \mathcal{D}\phi\, e^{-S_{\rm eff}[\phi,\xi]}, \tag{D1}$$

$$S_{\rm eff}[\phi,\xi] = S_0[\phi] + S_{\rm tun}[\phi] + \frac{1}{\beta} \sum_n \xi_{-n}\phi_n, \tag{D2}$$

$$S_0[\phi] = \sum_n \frac{|\phi_n|^2}{4\beta\Lambda_n}, \tag{D3}$$

$$S_{\rm tun}[\phi] = -V \int d\tau\, \cos\phi(\tau). \tag{D4}$$

The correlation function follows from functional differentiation

$$\langle \phi_n \phi_{-n} \rangle = \beta^2 \frac{\delta^2 \ln Z[\xi]}{\delta\xi_{-n}\delta\xi_n}\bigg|_{\xi=0}. \tag{D5}$$

For $V = 0$,

$$Z_0[\xi] = \exp\left(\frac{1}{\beta} \sum_n \Lambda_n \xi_n \xi_{-n}\right), \tag{D6}$$

yielding the noninteracting correlator

$$\langle \phi_n \phi_{-n} \rangle_0 = 2\beta\Lambda_n. \tag{D7}$$

Expanding in $S_{\rm tun}$,

$$e^{-S_0 - S_{\rm tun}} = e^{-S_0}\left(1 - S_{\rm tun} + \tfrac{1}{2}S_{\rm tun}^2 + \cdots\right), \tag{D8}$$

the first-order contribution to the generating functional reads

$$Z_1[\xi] = V \int \mathcal{D}\phi \int d\tau\, \cos\phi\, e^{-S_0[\phi] - \beta^{-1}\sum_n \xi_{-n}\phi_n}. \tag{D9}$$

Performing standard Gaussian integration of the ϕ field yields

$$\left.\frac{Z_1}{Z_0}\right|_{\xi=0} = \beta V e^{-\bar{\Lambda}}, \tag{D10}$$

$$\left.\frac{1}{Z_0}\frac{\delta^2 Z_1}{\delta\xi_{-n}\delta\xi_n}\right|_{\xi=0} = 2Ve^{-\bar{\Lambda}}\Lambda_n\left(1-\frac{2\Lambda_n}{\beta}\right), \tag{D11}$$

with $\bar{\Lambda} = \beta^{-1}\sum_p \Lambda_p$. The first-order correction to the correlation function thus reads

$$\langle\phi_n\phi_{-n}\rangle_1 = -4\beta V\Lambda_n^2 e^{-\bar{\Lambda}}. \tag{D12}$$

At second order, one has

$$Z_2[\xi] = \frac{V^2}{2}\int\mathcal{D}\phi\int d\tau d\tau'\,\cos\phi(\tau)\cos\phi(\tau')e^{-S_0[\phi]-\beta^{-1}\sum_n\xi_{-n}\phi_n}. \tag{D13}$$

Again, performing the Gaussian integration over ϕ gives

$$\left.\frac{Z_2}{Z_0}\right|_{\xi=0} = +\frac{\beta V^2}{4}e^{-2\bar{\Lambda}}[\mathcal{P}_+(0)+\mathcal{P}_-(0)], \tag{D14}$$

$$\left.\frac{1}{Z_0}\frac{\delta^2 Z_2}{\delta\xi_{-n}\delta\xi_n}\right|_{\xi=0} = \frac{\Lambda_n V^2}{2}e^{-2\bar{\Lambda}}\left\{\left(1-\frac{4\Lambda_n}{\beta}\right)[\mathcal{P}_+(0)+\mathcal{P}_-(0)]+\frac{4\Lambda_n}{\beta}[\mathcal{P}_+(i\omega_n)-\mathcal{P}_-(i\omega_n)]\right\}, \tag{D15}$$

where $\mathcal{P}_\pm(\omega_n)$ is defined in Eq. (42). The second-order correction to the correlation function becomes

$$\langle\phi_n\phi_{-n}\rangle_2 = -2\beta V^2\Lambda_n^2 e^{-2\bar{\Lambda}}[\mathcal{P}_+(0)+\mathcal{P}_-(0)-\mathcal{P}_+(i\omega_n)+\mathcal{P}_-(i\omega_n)-2\beta]. \tag{D16}$$

For $s_1 = 0$ and $s_2 = L/2$, the interaction kernel takes the form

$$\Gamma(i\omega_n) = \frac{8\pi^2(\omega_T^2+\omega_n^2)}{\nu L^2}\left[\frac{1}{\omega_T}-\frac{\omega_T^2+\omega_n^2}{(\omega_T+\nu\beta\Phi)(\omega_T^2+\omega_n^2)+\nu\beta\Phi(\omega_T^2-\omega_n^2)}\right], \tag{D17}$$

where $\Phi(i\omega_n)$ was defined in Eq. (35). Expanding in V, we are left with

$$\Gamma(i\omega_n) = \left.\frac{\partial\Gamma}{\partial V}\right|_{V=0}V + \frac{1}{2}\left.\frac{\partial^2\Gamma}{\partial V^2}\right|_{V=0}V^2 + O(V^3). \tag{D18}$$

The coefficients of the expansion are then given by

$$\left.\frac{\partial\Gamma}{\partial V}\right|_{V=0} = \left.\frac{\partial\Gamma}{\partial\Phi}\frac{\partial\Phi}{\partial V}\right|_{V=0}, \tag{D19}$$

$$\left.\frac{\partial^2\Gamma}{\partial V^2}\right|_{V=0} = \left.\left(\frac{\partial^2\Phi}{\partial V^2}\frac{\partial\Gamma}{\partial\Phi}+\left(\frac{\partial\Phi}{\partial V}\right)^2\frac{\partial^2\Gamma}{\partial\Phi^2}\right)\right|_{V=0}, \tag{D20}$$

where the required derivatives read

$$\left.\frac{\partial\Gamma}{\partial\Phi}\right|_{V=0} = \frac{16\pi^2\beta}{L^2}, \tag{D21}$$

$$\left.\frac{\partial^2\Gamma}{\partial\Phi^2}\right|_{V=0} = -\frac{64\pi^2\nu\beta^2\omega_T}{L^2(\omega_T^2+\omega_n^2)}, \tag{D22}$$

$$\left.\frac{\partial\Phi}{\partial V}\right|_{V=0} = \frac{1}{\beta^2\Lambda_n^2}\frac{\langle\phi_n\phi_{-n}\rangle_1}{V}, \tag{D23}$$

$$\left.\frac{\partial^2\Phi}{\partial V^2}\right|_{V=0} = \frac{2}{\beta^2\Lambda_n^2}\frac{\langle\phi_n\phi_{-n}\rangle_2}{V^2}. \tag{D24}$$

Substituting these back into Eq. (D18) and using Eqs. (D12) and (D16) reproduces the result of Eq. (41).

[1] D. C. Tsui, H. L. Stormer, and A. C. Gossard, Two-dimensional magnetotransport in the extreme quantum limit, Phys. Rev. Lett. **48**, 1559 (1982).

[2] R. B. Laughlin, Anomalous quantum Hall effect: An incompressible quantum fluid with fractionally charged excitations, Phys. Rev. Lett. **50**, 1395 (1983).

[3] B. I. Halperin, Quantized Hall conductance, current-carrying edge states, and the existence of extended states in a two-dimensional disordered potential, Phys. Rev. B **25**, 2185 (1982).

[4] L. Saminadayar, D. C. Glattli, Y. Jin, and B. Etienne, Observation of the $e/3$ fractionally charged Laughlin quasiparticle, Phys. Rev. Lett. **79**, 2526 (1997).

[5] R. de-Picciotto, M. Reznikov, M. Heiblum, V. Umansky, G. Bunin, and D. Mahalu, Direct observation of a fractional charge, Nature (London) **389**, 162 (1997).

[6] F. Wilczek, Quantum mechanics of fractional-spin particles, Phys. Rev. Lett. **49**, 957 (1982).

[7] D. Arovas, J. R. Schrieffer, and F. Wilczek, Fractional statistics and the quantum Hall effect, Phys. Rev. Lett. **53**, 722 (1984).

[8] C. Nayak, S. H. Simon, A. Stern, M. Freedman, and S. Das Sarma, Non-Abelian anyons and topological quantum computation, Rev. Mod. Phys. **80**, 1083 (2008).

[9] A. Stern, Anyons and the quantum Hall effect: A pedagogical review, Ann. Phys. **323**, 204 (2008).

[10] D. E. Feldman and B. I. Halperin, Fractional charge and fractional statistics in the quantum Hall effects, Rep. Prog. Phys. **84**, 076501 (2021).

[11] J. Nakamura, S. Liang, G. C. Gardner, and M. J. Manfra, Direct observation of anyonic braiding statistics, Nat. Phys. **16**, 931 (2020).

[12] H. Bartolomei, M. Kumar, R. Bisognin, A. Marguerite, J.-M. Berroir, E. Bocquillon, B. Plaçais, A. Cavanna, Q. Dong, U. Gennser, *et al.*, Fractional statistics in anyon collisions, Science **368**, 173 (2020).

[13] M. Carrega, L. Chirolli, S. Heun, and L. Sorba, Anyons in quantum Hall interferometry, Nat. Rev. Phys. **3**, 698 (2021).

[14] J. Nakamura, S. Liang, G. C. Gardner, and M. J. Manfra, Fabry-Pérot interferometry at the $\nu = 2/5$ fractional quantum Hall state, Phys. Rev. X **13**, 041012 (2023).

[15] H. K. Kundu, S. Biswas, N. Ofek, V. Umansky, and M. Heiblum, Anyonic interference and braiding phase in a Mach-Zehnder interferometer, Nat. Phys. **19**, 515 (2023).

[16] R. L. Willett, K. Shtengel, C. Nayak, L. N. Pfeiffer, Y. J. Chung, M. L. Peabody, K. W. Baldwin, and K. W. West, Interference measurements of non-Abelian $e/4$ & Abelian $e/2$ quasiparticle braiding, Phys. Rev. X **13**, 011028 (2023).

[17] N. Batra, Z. Wei, S. Vishveshwara, and D. E. Feldman, Anyonic Mach-Zehnder interferometer on a single edge of a two-dimensional electron gas, Phys. Rev. B **108**, L241302 (2023).

[18] T. Werkmeister, J. R. Ehrets, Y. Ronen, M. E. Wesson, D. Najafabadi, Z. Wei, K. Watanabe, T. Taniguchi, D. E. Feldman, B. I. Halperin, *et al.*, Strongly coupled edge states in a graphene quantum Hall interferometer, Nat. Commun. **15**, 6533 (2024).

[19] T. Werkmeister, J. R. Ehrets, M. E. Wesson, D. H. Najafabadi, K. Watanabe, T. Taniguchi, B. I. Halperin, A. Yacoby, and P. Kim, Anyon braiding and telegraph noise in a graphene interferometer, Science **388**, 730 (2025).

[20] B. Rosenow, I. P. Levkivskyi, and B. I. Halperin, Current correlations from a mesoscopic anyon collider, Phys. Rev. Lett. **116**, 156802 (2016).

[21] C. Han, J. Park, Y. Gefen, and H. S. Sim, Topological vacuum bubbles by anyon braiding, Nat. Commun. **7**, 11131 (2016).

[22] C. Mora, Anyonic exchange in a beam splitter, arXiv:2212.05123.

[23] T. Morel, J.-Y. M. Lee, H.-S. Sim, and C. Mora, Fractionalization and anyonic statistics in the integer quantum Hall collider, Phys. Rev. B **105**, 075433 (2022).

[24] J.-Y. M. Lee and H. S. Sim, Non-Abelian anyon collider, Nat. Commun. **13**, 6660 (2022).

[25] M. Ruelle, E. Frigerio, J.-M. Berroir, B. Plaçais, J. Rech, A. Cavanna, U. Gennser, Y. Jin, and G. Fève, Comparing fractional quantum Hall Laughlin and Jain topological orders with the anyon collider, Phys. Rev. X **13**, 011031 (2023).

[26] P. Glidic, O. Maillet, A. Aassime, C. Piquard, A. Cavanna, U. Gennser, Y. Jin, A. Anthore, and F. Pierre, Cross-correlation investigation of anyon statistics in the $\nu = 1/3$ and $2/5$ fractional quantum Hall states, Phys. Rev. X **13**, 011030 (2023).

[27] T. Jonckheere, J. Rech, B. Grémaud, and T. Martin, Anyonic statistics revealed by the Hong-Ou-Mandel dip for fractional excitations, Phys. Rev. Lett. **130**, 186203 (2023).

[28] N. Schiller, Y. Shapira, A. Stern, and Y. Oreg, Anyon statistics through conductance measurements of time-domain interferometry, Phys. Rev. Lett. **131**, 186601 (2023).

[29] J.-Y. M. Lee, C. Hong, T. Alkalay, N. Schiller, V. Umansky, M. Heiblum, Y. Oreg, and H. S. Sim, Partitioning of diluted anyons reveals their braiding statistics, Nature (London) **617**, 277 (2023).

[30] K. Iyer, F. Ronetti, B. Grémaud, T. Martin, J. Rech, and T. Jonckheere, Finite width of anyons changes their braiding signature, Phys. Rev. Lett. **132**, 216601 (2024).

[31] M. Thamm and B. Rosenow, Effect of the soliton width on nonequilibrium exchange phases of anyons, Phys. Rev. Lett. **132**, 156501 (2024).

[32] F. Ronetti, N. Demazure, J. Rech, T. Jonckheere, B. Grémaud, L. Raymond, M. Hashisaka, T. Kato, and T. Martin, Anyon braiding on the single edge of a fractional quantum Hall state, Phys. Rev. Lett. **135**, 146601 (2025).

[33] F. Ronetti, N. Demazure, J. Rech, T. Jonckheere, B. Grémaud, L. Raymond, M. Hashisaka, T. Kato, and T. Martin, Probing anyon statistics on a single-edge loop in the fractional quantum Hall regime, Phys. Rev. B **112**, 125166 (2025).

[34] M. Ruelle, E. Frigerio, E. Baudin, J.-M. Berroir, B. Plaçais, B. Grémaud, T. Jonckheere, T. Martin, J. Rech, A. Cavanna, *et al.*, Time-domain braiding of anyons, Science **389**, eadm7695 (2025).

[35] H. Saleur, Edge states tunneling in the fractional quantum Hall effect: Integrability and transport, C. R. Phys. **3**, 685 (2002).

[36] D. C. Glattli, Tunneling experiments in the fractional quantum Hall effect regime, in *The Quantum Hall Effect: Poincaré Seminar 2004*, edited by B. Douçot, V. Pasquier, B. Duplantier, and V. Rivasseau (Birkhäuser Basel, Basel, 2005), pp. 163–197.

[37] V. Volkov and S. A. Mikhailov, Edge magnetoplasmons: Low frequency weakly damped excitations in inhomogeneous two-dimensional electron systems, Zh. Eksp. Teor. Fiz. **94**, 217 (1988) [Sov. Phys. JETP **67**, 1639 (1988)].

[38] E. Andrei, D. Glattli, F. Williams, and M. Heiblum, Low frequency collective excitations in the quantum-Hall system, Surf. Sci. **196**, 501 (1988).

[39] V. Talyanskii, M. Wassermeier, A. Wixforth, J. Oshinowo, J. Kotthaus, I. Batov, G. Weimann, H. Nickel, and W. Schlapp, Edge magnetoplasmons in the quantum Hall effect regime, Surf. Sci. **229**, 40 (1990).

[40] R. C. Ashoori, H. L. Stormer, L. N. Pfeiffer, K. W. Baldwin, and K. West, Edge magnetoplasmons in the time domain, Phys. Rev. B **45**, 3894 (1992).

[41] N. B. Zhitenev, R. J. Haug, K. v. Klitzing, and K. Eberl, Experimental determination of the dispersion of edge magnetoplasmons confined in edge channels, Phys. Rev. B **49**, 7809 (1994).

[42] N. Kumada, H. Kamata, and T. Fujisawa, Edge magnetoplasmon transport in gated and ungated quantum Hall systems, Phys. Rev. B **84**, 045314 (2011).

[43] I. Petković, F. I. B. Williams, K. Bennaceur, F. Portier, P. Roche, and D. C. Glattli, Carrier drift velocity and edge magnetoplasmons in graphene, Phys. Rev. Lett. **110**, 016801 (2013).

[44] M. Hashisaka, H. Kamata, N. Kumada, K. Washio, R. Murata, K. Muraki, and T. Fujisawa, Distributed-element circuit model of edge magnetoplasmon transport, Phys. Rev. B **88**, 235409 (2013).

[45] N. Kumada, P. Roulleau, B. Roche, M. Hashisaka, H. Hibino, I. Petković, and D. C. Glattli, Resonant edge magnetoplasmons and their decay in graphene, Phys. Rev. Lett. **113**, 266601 (2014).

[46] A. Endo, K. Koike, S. Katsumoto, and Y. Iye, Frequencies of the edge-magnetoplasmon excitations in gated quantum Hall edges, J. Phys. Soc. Jpn. **87**, 064709 (2018).

[47] A. C. Mahoney, J. I. Colless, S. J. Pauka, J. M. Hornibrook, J. D. Watson, G. C. Gardner, M. J. Manfra, A. C. Doherty, and D. J. Reilly, On-chip microwave quantum Hall circulator, Phys. Rev. X **7**, 011007 (2017).

[48] S. Bosco, D. P. DiVincenzo, and D. J. Reilly, Transmission lines and metamaterials based on quantum Hall plasmonics, Phys. Rev. Appl. **12**, 014030 (2019).

[49] E. Frigerio, G. Rebora, M. Ruelle, H. Souquet-Basiège, Y. Jin, U. Gennser, A. Cavanna, B. Plaçais, E. Baudin, J.-M. Berroir, *et al.*, Gate tunable edge magnetoplasmon resonators, Commun. Phys. **7**, 314 (2024).

[50] D. Ferraro, M. Carrega, A. Braggio, and M. Sassetti, Multiple quasiparticle Hall spectroscopy investigated with a resonant detector, New J. Phys. **16**, 043018 (2014).

[51] I. L. Drichko, A. M. Diakonov, V. A. Malysh, I. Y. Smirnov, Y. M. Galperin, N. D. Ilyinskaya, A. A. Usikova, M. Kummer, and H. von Känel, Contactless measurement of alternating current conductance in quantum Hall structures, J. Appl. Phys. **116**, 154309 (2014).

[52] J. Cano, A. C. Doherty, C. Nayak, D. J. Reilly, Microwave absorption by a mesoscopic quantum Hall droplet, Phys. Rev. B **88**, 165305 (2013).

[53] B. Oblak, B. Lapierre, P. Moosavi, J.-M. Stéphan, and B. Estienne, Anisotropic quantum Hall droplets, Phys. Rev. X **14**, 011030 (2024).

[54] C. L. Kane and M. P. A. Fisher, Contacts and edge-state equilibration in the fractional quantum Hall effect, Phys. Rev. B **52**, 17393 (1995).

[55] E. V. Deviatov, A. A. Kapustin, V. T. Dolgopolov, A. Lorke, D. Reuter, and A. D. Wieck, Equilibration between edge states in the fractional quantum Hall effect regime at high imbalances, Phys. Rev. B **74**, 073303 (2006).

[56] D. B. Mast, A. J. Dahm, and A. L. Fetter, Observation of bulk and edge magnetoplasmons in a two-dimensional electron fluid, Phys. Rev. Lett. **54**, 1706 (1985).

[57] D. C. Glattli, E. Y. Andrei, G. Deville, J. Poitrenaud, and F. I. B. Williams, Dynamical Hall effect in a two-dimensional classical plasma, Phys. Rev. Lett. **54**, 1710 (1985).

[58] A. M. Chang, Chiral Luttinger liquids at the fractional quantum Hall edge, Rev. Mod. Phys. **75**, 1449 (2003).

[59] X.-G. Wen, Theory of the edge states in fractional quantum Hall effects, Int. J. Mod. Phys. B **06**, 1711 (1992).

[60] M. R. Geller and D. Loss, Aharanov-Bohm effect in the chiral Luttinger liquid, Phys. Rev. B **56**, 9692 (1997).

[61] J. von Delft and H. Schoeller, Bosonization for beginners—Refermionization for experts, Ann. Phys. (Berlin) **510**, 225 (1998).

[62] D. Loss, Parity effects in a Luttinger liquid: Diamagnetic and paramagnetic ground states, Phys. Rev. Lett. **69**, 343 (1992).

[63] W. Magnus, On the exponential solution of differential equations for a linear operator, Commun. Pure Appl. Math. **7**, 649 (1954).

[64] K. Moon, H. Yi, C. L. Kane, S. M. Girvin, and M. P. A. Fisher, Resonant tunneling between quantum Hall edge states, Phys. Rev. Lett. **71**, 4381 (1993).

[65] F. Murabayashi, Code and data for "Microwave response of fractional quantum Hall droplets with quasiparticle tunneling" [Data set], Zenodo, 2026, https://doi.org/10.5281/zenodo.18933586.